Tropical nighttime warming as a dominant driver of variability in the terrestrial carbon sink

Supporting Information Text

Remote-sensing data and analyses

To estimate terrestrial gross primary productivity (GPP) for years in the satellite record (1982–2011), we used the MODIS GPP algorithm (1, 2). This method is based on the logic that GPP can be estimated as the total solar energy absorbed by a given area of vegetation over a given amount of time—obtained from satellite remote sensing—scaled by the efficiency with which the given area of vegetation is able to convert absorbed solar energy to usable energy (3):

$$GPP = \sum FPAR \times PAR \times LUE_{\max} \times f(T_{\min}) \times f(VPD) \quad \text{(Eq 1)}$$

Where *FPAR* represents the satellite-derived fraction of photosynthetically active radiation absorbed by the vegetation, *PAR* represents the total incoming shortwave radiation, LUE_{max} represents biome-specific maximum light use efficiency, $f(T_{min})$ represents a low-temperature stress-reduction scalar, and $f(VPD)$ represents a water stress reduction scalar. *FPAR* satellite data were derived from the newly available gridded Global Inventory Modeling and Mapping Studies (GIMMS) FPAR3g dataset (4); while daily gridded meteorological variables *PAR*, *Tmin*, and *VPD* were obtained from the NCEP/DOE reanalysis II model (5). Uncertainty bounds calculated for satellite GPP data represent the full range of potential parameter combinations for meteorological drivers

22 $f(T_{min})$ and $f(VPD)$, which enabled a focus on the actual satellite signal. All
23 meteorological variables were resampled using bilinear interpolation to match the ~8-km
24 spatial resolution of the satellite data. Biome-specific properties, such as $LUE_{max,}$ were
25 mapped using the MODIS MCD12 dataset with the University of Maryland (UMD) land
26 cover classification system (6). We aggregated GPP by long-term climate zone,
27 according to the Köppen-Geiger climate classification (7).
28 We emphasize that while estimates of GPP are derived from and partially
29 dependent on climate data, the trends in variance that we report globally and within
30 biomes are visible in the raw satellite data (Fig S7). This provides strong evidence that
31 the decrease in variance of GPP over the 1982–2011 window is not driven by
32 confounding effects of climate in GPP's formulation, but instead by robust trends in the
33 satellite data.
34 We compared our results on interannual variability in satellite-derived GPP to
35 previous work (8) based on upscaled flux tower data (flux-derived GPP (9)). While we
36 found similar increases in variability in GPP across arid climate zones, we found a starkly
37 contrasting trend of decreasing variance in the satellite-derived GPP estimates at the
38 global scale and for all other climate zones. We note that our satellite-derived GPP
39 estimates are based on the latest, third-generation merged satellite FPAR3g product,
40 which features improved data quality and algorithm calibration (4); while the flux-
41 derived GPP estimates are partially based on an earlier, first-generation merged satellite
42 product (9). In addition, methods limitations to flux tower-based estimates and relatively
43 low sample density of flux towers in these tropical regions also limit our confidence of
44 GPP estimates. These findings highlight the critical need for future research aimed at

45 reducing uncertainties and resolving this apparent discrepancy in our best long-term,
46 observation-based GPP datasets.
47
48 *Disturbance and fire analyses*
49 Fire is one of the major ecosystem disturbances that can affect the land carbon
50 balance. CO_2 and other carbon-containing compounds are by-products of combustion,
51 estimated to total around 2.0 to 2.5 PgC yr^{-1} in the early 2000s (10, 11). Decomposition
52 of fire-killed vegetation adds more emissions over a longer time period. However,
53 vegetation regrowth following fire might be expected to result in no net effect on the
54 carbon cycle when averaged over a long time period. Burned ecosystems also have less
55 biomass that gets respired and/or emitted during land-use change. In sum, without fire, it
56 has been estimated that the net carbon flux from the land to the atmosphere would
57 actually have been about 1 Pg yr^{-1} higher across the 20th century (12).
58 Unfortunately, the quality of long-term datasets regarding the amount of fire and
59 associated emissions is poor due to a number of factors. Perhaps chief among these is the
60 fact that reliable estimates of burned area at a global scale only extend as far back as the
61 mid- to late-1990s, when moderate-resolution imaging satellites began coming online.
62 Governments in some regions (namely Alaska, Canada, and Siberia) have kept records of
63 large vegetation fires since the mid-20th century, but even those data carry large
64 uncertainties due to the remoteness of some fires, among other reasons (13). Translating
65 burned area into emissions also presents a challenge, since the relationship between the
66 two varies widely across different regions, ecosystem types, and weather conditions (14).
67 Incorporating simulations of burned area and emissions into Earth system models could

68 improve our understanding of trends and interannual variability, but only a few long-term
69 reconstructions have been produced (12, 14, 15), and it is often difficult for such models
70 to recreate extreme fire years.

71 Figure S10 shows, for the period of our study, several reconstructed time-series of
72 fire emissions (specifically, C from CO_2) in terms of deviation from their respective
73 means. The Global Inventory for Chemistry-Climate studies (GICC(16)) estimated
74 emissions (for 1900–1996 based on burned area estimates from Mouillot & Field (2005)
75 (17), and for 1997–2005 using satellite data), based on a vegetation type distribution from
76 the year 2000 and assuming characteristic emissions per burned area for each vegetation
77 type. Because of the qualitative nature of their methodology in most regions, Mouillot &
78 Field (2005) only produced decadal burned area estimates, and therefore there is no
79 attempt to capture interannual variability across the time-series. The Atmospheric
80 Chemistry and Climate Model Intercomparison Project (ACCMIP (18)) based its time-
81 series for 1900–1959 on that of GICC, with a modification to allow for greater emissions
82 from peatland fires. For the rest of the 20th century, ACCMIP used a decadally-averaged
83 version of the RETRO database (14), which combined a mechanistic model of fire
84 occurrence and emissions with, when available, country-level fire inventory data and
85 satellite observations of burned area to generate an emissions time-series covering 1960–
86 2000. Yue et al. (2014) also used a mechanistic fire model, integrating it with a global
87 vegetation model to estimate burned area across the 20th century by forcing it with
88 climate reanalysis data and other observational datasets (15). That model also generates
89 emissions estimates, which are shown in Figure S10. Finally, we included a time series
90 from version 3 of the Global Fire Emissions Database (GFED3) (10), which combines

satellite observations of burned area with a vegetation model to generate emissions estimates. (ACCMIP used GFED version 2 for emissions in 2000, and used that year to harmonize the other two time-series it incorporated.)

Because of the relatively low quality of data available regarding the amount, distribution, and interannual variability of carbon losses from fire, we did not explicitly include fire activity as a driver of the land carbon sink in our analysis. That said, the land use emissions estimates we used (from the bookkeeping method and two vegetation models) incorporate some global fire emissions indirectly—tropical deforestation and degradation fires accounted for about 20% of annual emissions from burning across 2001–2009 (10). In addition, we compared the interannual variability of the RETRO and GFED fire emissions data to terrestrial NEE. The correlations of NEE were non-significant ($p=0.06$) with the RETRO data and were significant with the GFED3 database ($p=0.01$), but the latter result was likely due to the presence of the outlier year 1998 (Fig S11). Without this severe year, the relationship is non-significant ($p=0.12$). Thus, currently available data indicate that NEE interannual variability is not tightly coupled to fire emissions data, but a full test of fire's role is not currently possible due to data limitations.

References

1. Running SW, et al. (2004) A continuous satellite-derived measure of global terrestrial primary production. *Bioscience* 54(6):547–560.

2. Zhao M, Running SW (2010) Drought-Induced Reduction in Global Terrestrial Net Primary Production from 2000 Through 2009. *Science* 329(5994):940–943.

3. Monteith J (1972) Solar radiation and productivity in tropical ecosystems. *J Appl Ecol* 9(3):747–766.

4. Zhu Z, et al. (2013) Global data sets of vegetation leaf area index (LAI) 3g and Fraction of Photosynthetically Active Radiation (FPAR) 3g derived from Global Inventory Modeling and Mapping Studies (GIMMS) Normalized Difference Vegetation Index (NDVI3g) for the period 1981 to 2011. *Remote Sens* 5(2):927–948.

5. Kanamitsu M, et al. (2002) NCEP–DOE AMIP-II Reanalysis (R-2). *Bull Am Meteorol Soc* 83(11).

6. Friedl MA, et al. (2010) MODIS Collection 5 global land cover: Algorithm refinements and characterization of new datasets. *Remote Sens Environ* 114(1):168–182.

7. Peel MC, Finlayson BL, McMahon TA (2007) Updated world map of the Köppen-Geiger climate classification. *Hydrol Earth Syst Sci Discuss* 4(2).

8. Ahlström A, et al. (2015) The dominant role of semi-arid ecosystems in the trend and variability of the land CO2 sink. *Science* 348(6237):895–899.

9. Jung M, et al. (2011) Global patterns of land-atmosphere fluxes of carbon dioxide, latent heat, and sensible heat derived from eddy covariance, satellite, and meteorological observations. *J Geophys Res Biogeosciences 2005–2012* 116(G3). Available at: http://onlinelibrary.wiley.com/doi/10.1029/2010JG001566/full [Accessed May 28, 2015].

10. Van der Werf GR, et al. (2010) Global fire emissions and the contribution of deforestation, savanna, forest, agricultural, and peat fires (1997–2009). *Atmospheric Chem Phys* 10(23):11707–11735.

11. Randerson J, Chen Y, Werf G, Rogers B, Morton D (2012) Global burned area and biomass burning emissions from small fires. *J Geophys Res Biogeosciences 2005–2012* 117(G4).

12. Li F, Bond-Lamberty B, Levis S (2013) Quantifying the role of fire in the Earth system–Part 2: Impact on the net carbon balance of global terrestrial ecosystems for the 20th century. *Biogeosciences Discuss* 10(11):17309–17350.

13. Kasischke ES, Williams D, Barry D (2002) Analysis of the patterns of large fires in the boreal forest region of Alaska. *Int J Wildland Fire* 11(2):131–144.

14. Schultz MG, et al. (2008) Global wildland fire emissions from 1960 to 2000. *Glob Biogeochem Cycles* 22(2).

15. Yue C, et al. (2014) Modelling fires in the terrestrial carbon balance by incorporating SPITFIRE into the global vegetation model ORCHIDEE–Part 1: Simulating historical global burned area and fire regime. *Geosci Model Dev Discuss* 7(2):2377–2427.

16. Mieville A, et al. (2010) Emissions of gases and particles from biomass burning during the 20th century using satellite data and an historical reconstruction. *Atmos Environ* 44(11):1469–1477.

17. Mouillot F, Field CB (2005) Fire history and the global carbon budget: a 1× 1 fire history reconstruction for the 20th century. *Glob Change Biol* 11(3):398–420.

18. Lamarque J-F, et al. (2010) Historical (1850–2000) gridded anthropogenic and biomass burning emissions of reactive gases and aerosols: methodology and application. *Atmospheric Chem Phys* 10(15):7017–7039.

SI Tables

Table S1: Top-performing models from stepwise AIC model selection of all 12 climate drivers of terrestrial NEE calculated as residual of six ocean uptake models, after removing co-varying variables at r>0.5. ΔAIC is the difference in AIC from the base model with all variables included. Coefficients listed in the final model.

Model	**ΔAIC**
NEE ~ Tmin-Tropics + SaP1 + TropP + NorthT + SaT	-19.9
NEE ~ Tmin-Tropics + SaP1 + TropP + NorthT	-21.4
NEE ~ Tmin-Tropics + SaP1 + TropP	-22.4
NEE = -0.6*Tmin-Tropics + 0.3*SaP1	-23.8

183 Table S2: Top-performing models from stepwise AIC model selection of all 12 climate
184 drivers of terrestrial NEE calculated as residual of ocean data assimilation estimate, after
185 removing co-varying variables at r>0.5. ΔAIC is the difference in AIC from the base
186 model with all variables included. Coefficients listed in the final model.

Model	**ΔAIC**
NEE ~ Tmin-Tropics + SaP1 + TropP + GlobeP + SaT	-16.8
NEE ~ Tmin-Tropics + SaP1 + TropP + GlobeP	-18.3
NEE ~ Tmin-Tropics + SaP1 + TropP	-19.5
NEE = -0.6*Tmin-Tropics + 0.2*SaP1	-20.8

187

188

189 Table S3: Top-performing models from stepwise AIC model selection of climate

190 variables versus terrestrial respiration ($R = NEE_{GCP} - GPP$), where NEE is calculated

191 from the ocean models in the Global Carbon Project, after removing co-varying variables

192 at r>0.5.

Model	**AIC**
R ~ Precip-Tropics + Precip-North + GlobeT + Tmin-Tropics	3.97
R ~ Precip-North + GlobeT + Tmin-Tropics	2.14
R ~ Precip-North + Tmin-Tropics	0.42
R ~ Tmin-Tropics	-0.53

193

194

SI Figure Legends and Figures

Figure S1: Wavelet transformed power-spectra of terrestrial net ecosystem exchange (NEE). (Left) Morlet wavelet transformations, which gives higher resolution in the frequency (1/period) domain, for detrended NEE values (top) and detrended NEE with volcanic and ENSO signals removed (bottom). (Right) Mexican hat wavelet transformations, which gives higher resolution in the time domain, for detrended NEE values (top) and detrended NEE with volcanic and ENSO signals removed (bottom). Colors indicate intensity.

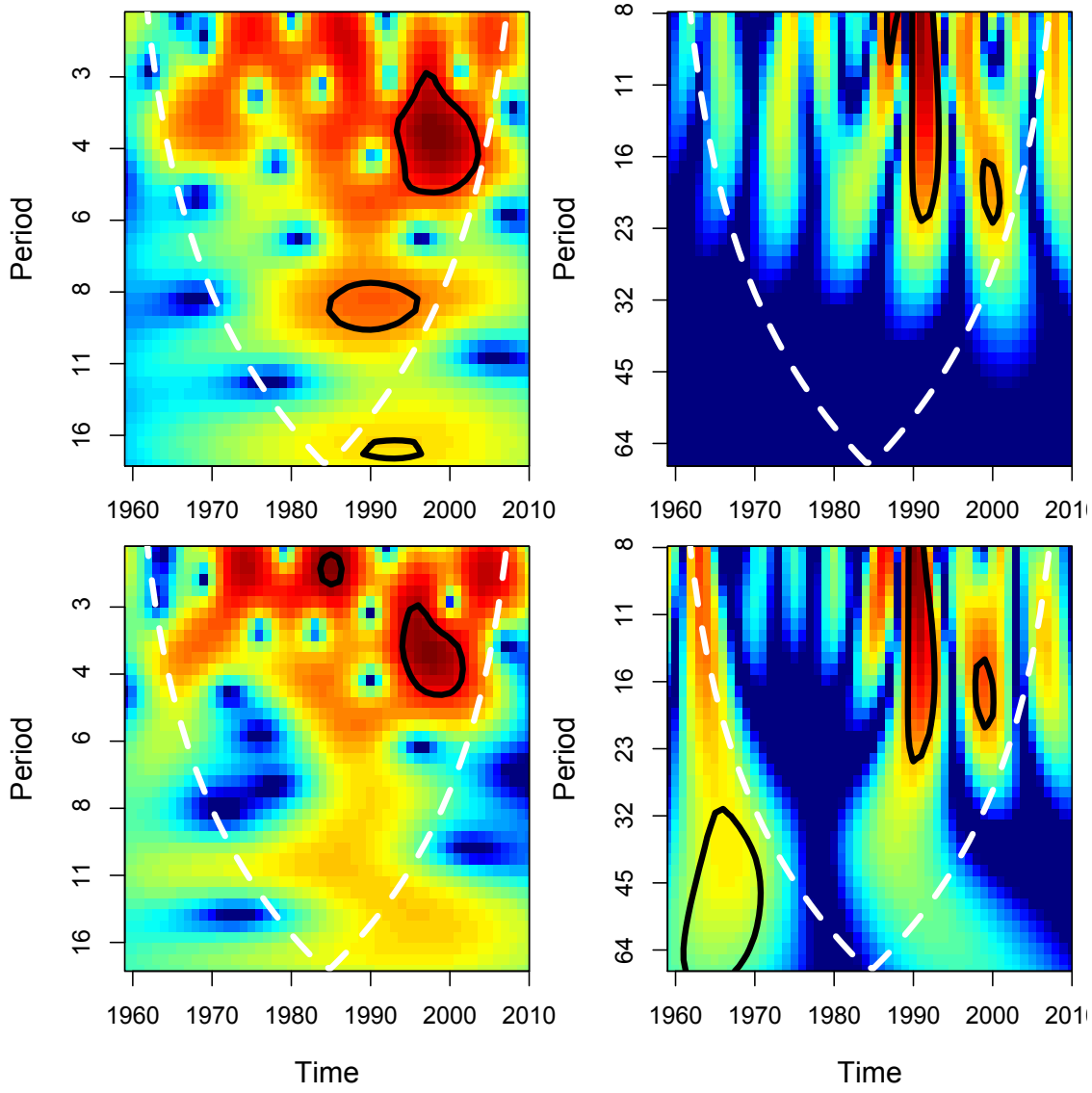

Figure S2: Trend in coefficient of variation of mean values of terrestrial carbon uptake, using 20-year moving windows (blue) and 10-year moving windows (black).

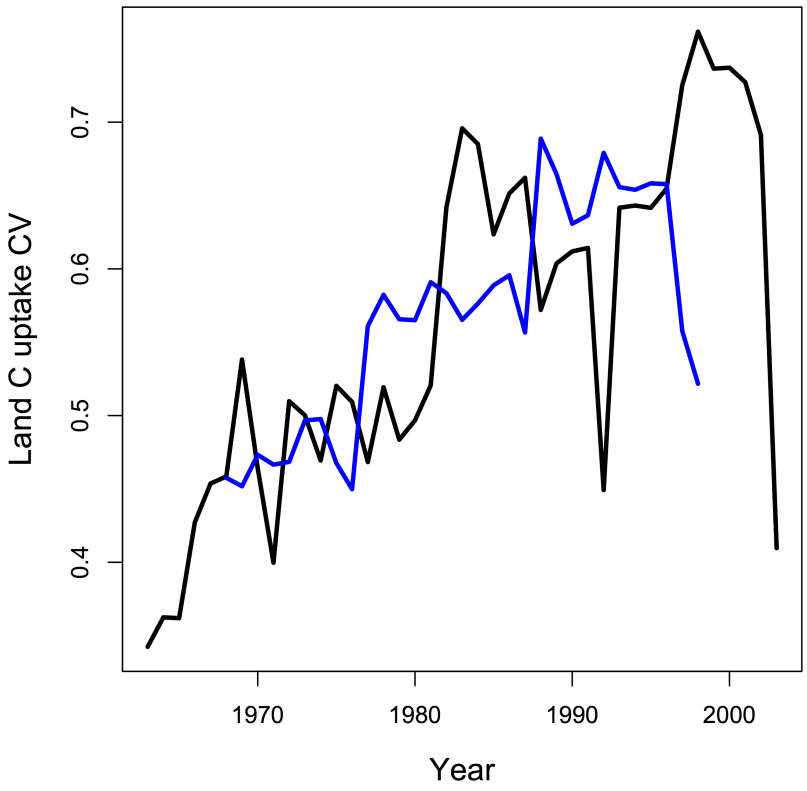

Figure S3: Time-series in variance of atmospheric growth rate of carbon dioxide, using NOAA global estimate (black) and Mauna Loa observatory (blue) using 20-year moving windows.

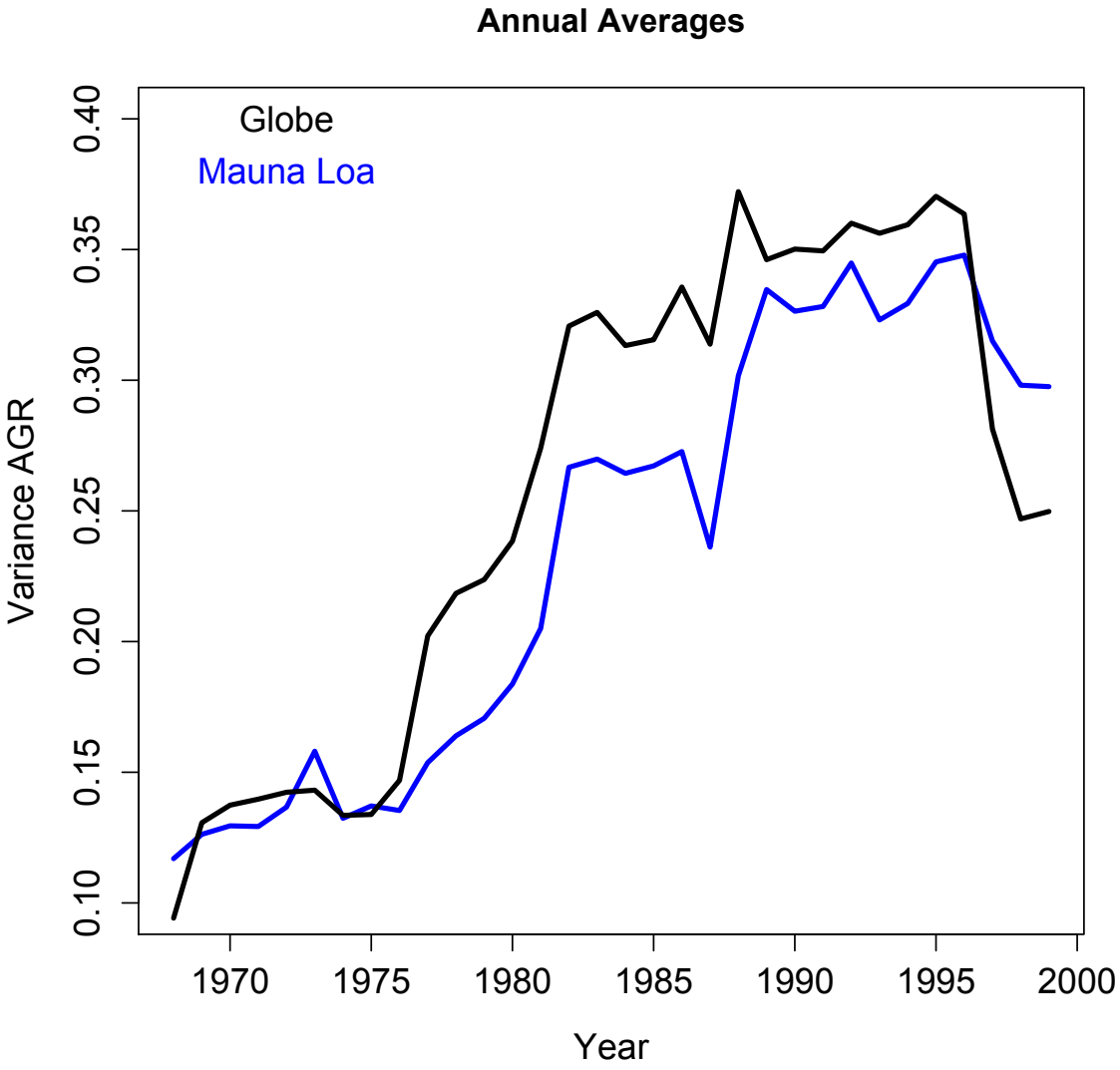

Figure S4: (a) Time-series in standard deviation of terrestrial NEE (black) with volcanic forcing removed (blue), ENSO removed (green), and both volcanic forcing and ENSO removed (red) using 10-year moving windows.

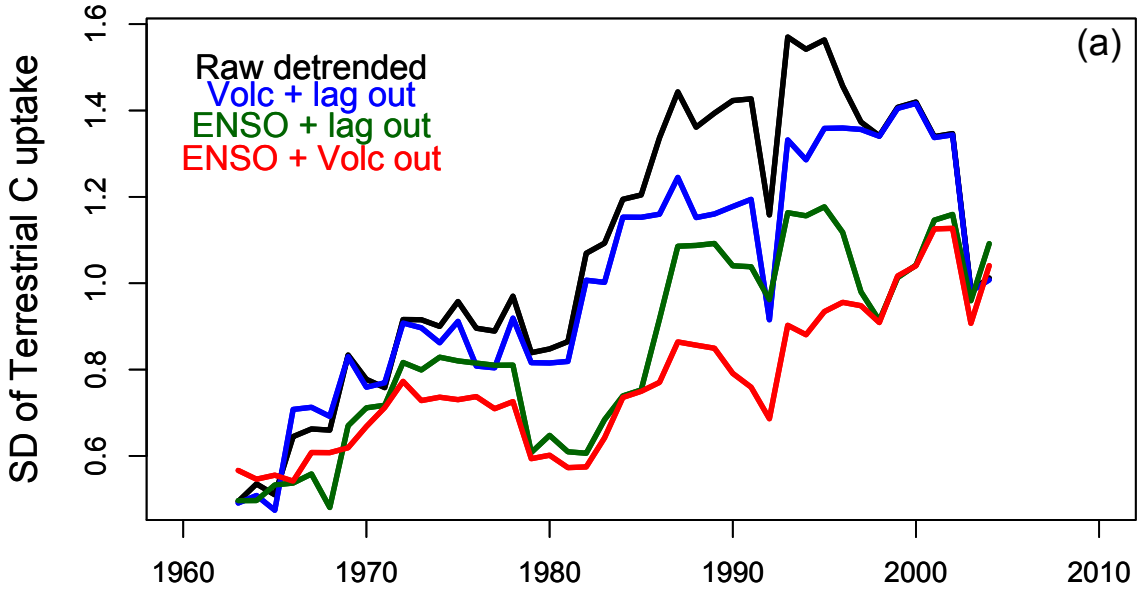

Figure S5: Interannual variability in the terrestrial C sink (NEE) is associated with nighttime tropical temperatures. All variables were detrended prior to analyses. (a) Partial correlations and their statistical significance (* is p <0.05) for each variable against NEE while conditioning on all other variables. Variables are minimum (nighttime) tropical temperatures (TropTmn), average tropical temperatures (TropT), maximum tropical temperatures (TropTmx), global average temperature (GlobT), average temperature of latitudes >30N (NorT), precipitation for the globe (GlobP), tropical regions (TropP), Northern extra-tropics (NorP), Semi-arid temperature (SaT) and 1 year lag (SaT1), and semi-arid precipitation (SaP) and 1 year lag (SaP1). (b) Trend in 20-year moving windows of partial correlation between terrestrial NEE_{AOGCM} and nighttime tropical temperatures when accounting for (red) daytime maximum tropical temperatures, solar radiation, and tropical precipitation; (black) global mean annual temperature, solar radiation, and tropical precipitation.

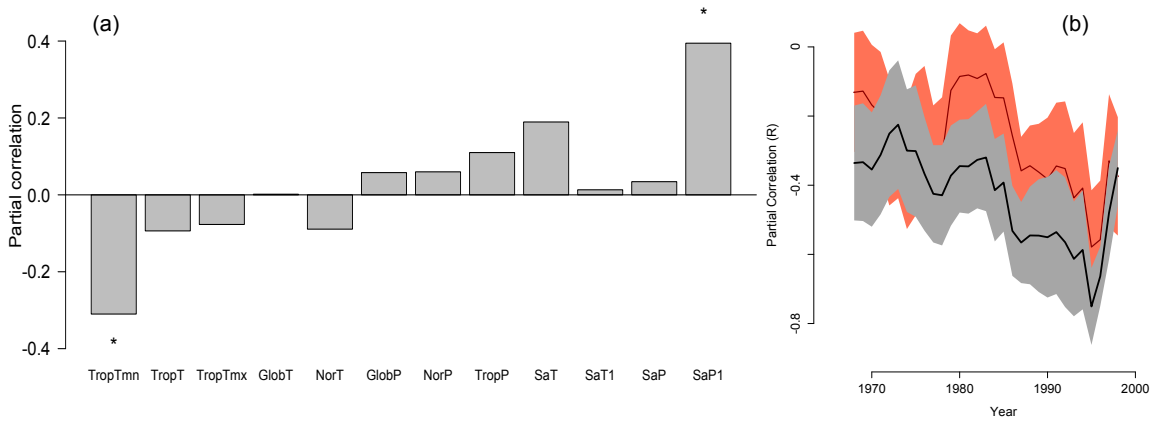

Figure S6: Interannual variability of net ecosystem exchange (NEE) is driven primarily by tropical nighttime temperature. Probability density of the relative likelihoods determined by AIC of each model of NEE as a function of minimum (nighttime) tropical temperatures (TropTmn), average tropical temperatures (TropT), maximum tropical temperatures (TropTmx), global average temperature (GlobT), average temperature of latitudes >30ºN (NorT), global land precipitation (GlobP), tropical land precipitation (TropP), Northern extra-tropics land precipitation (NorP), average temperature for semi-arid regions (SaT) and with a one year lag (SaT1), and average precipitation for semi-arid regions (SaP) and with a one year lag (SaP1). Black bars indicate median relative likelihood of the single-variable model.

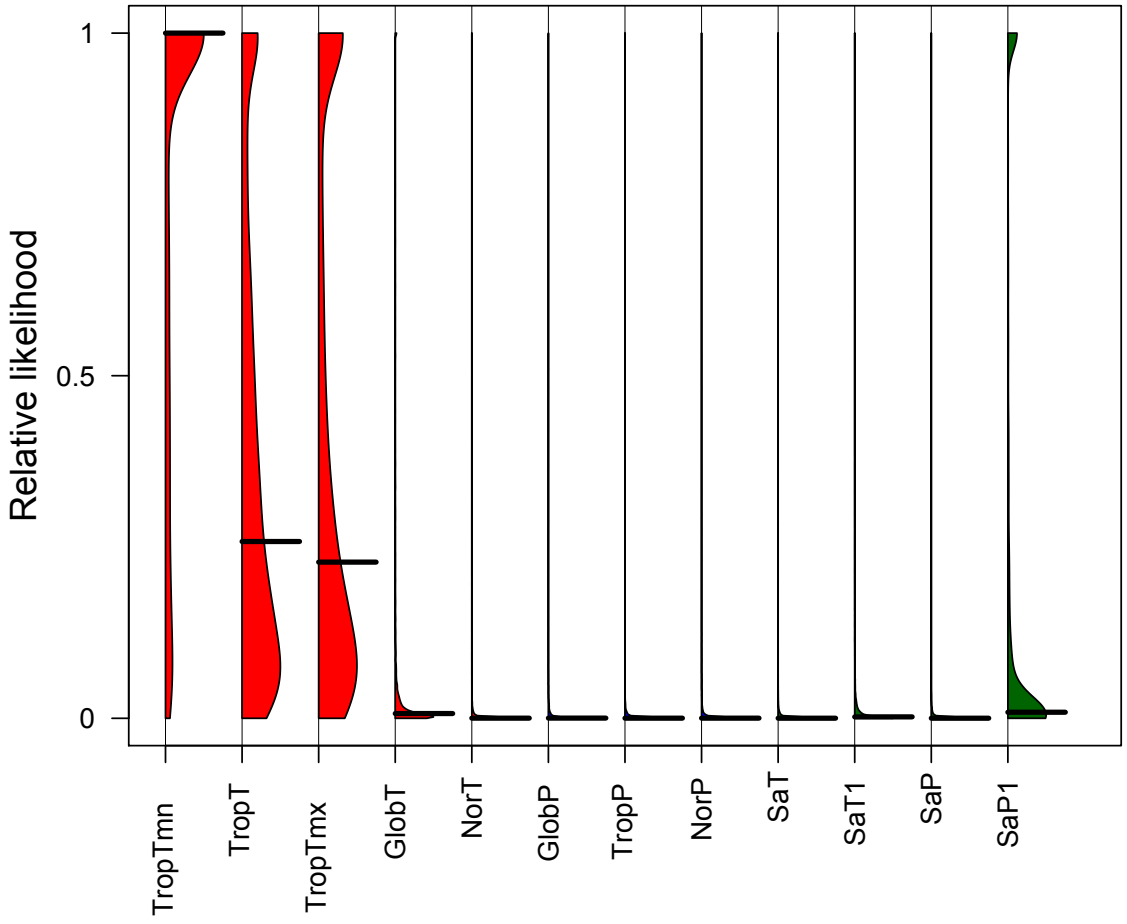

Figure S7: Declining variability of satellite-derived GPP. Moving 10-year windows of standard deviation of satellite-derived GPP (solid line), flux-derived GPP (thin dashes), and FPAR3g (thick dashes) from 1982–2011 for (a) the globe, (b) tropical regions, (c) temperate regions, (d) arid regions, and (e) cold regions. Shaded interval shows the full distribution of uncertainty due to climate inputs in the satellite-derived GPP algorithm and straight lines give the best fit via ordinary least-squares regression.

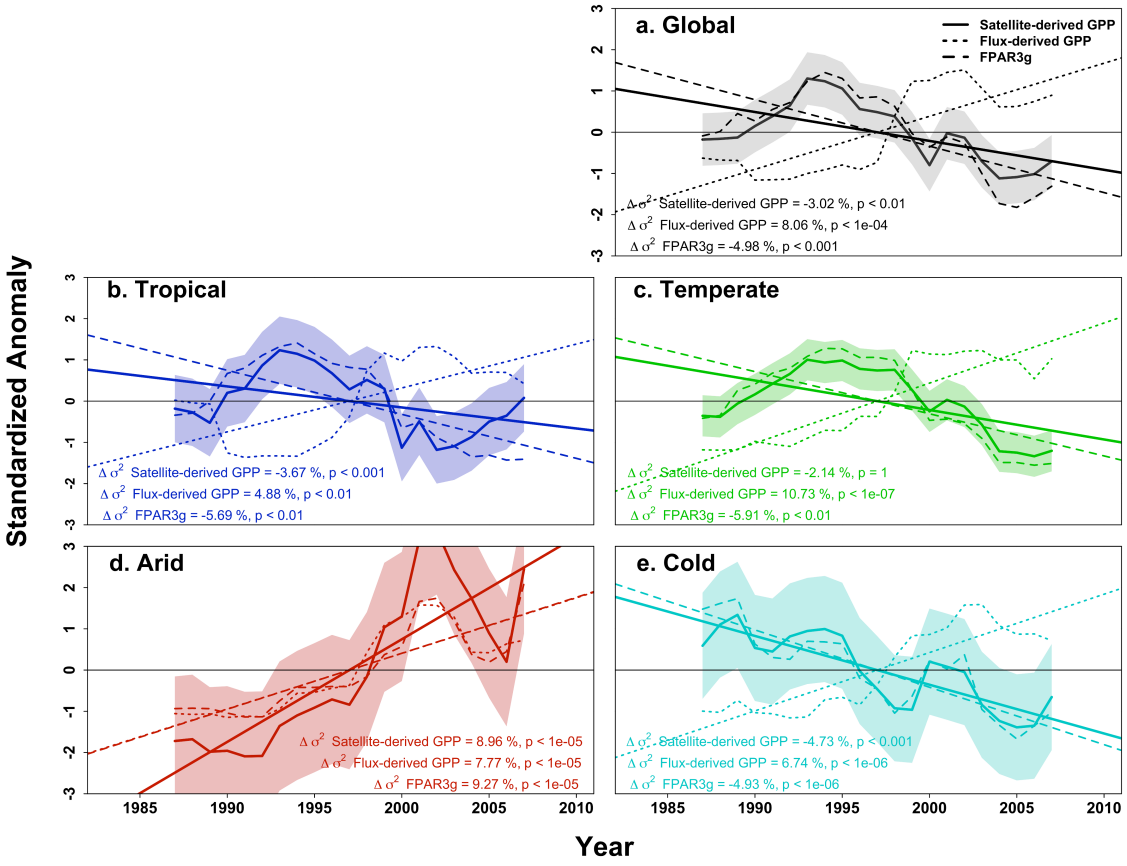

Figure S8: Global respiration is driven primarily by tropical nighttime temperature. (a) Standardized anomaly (Z-score) of detrended global terrestrial respiration (blue) and detrended tropical nighttime temperature (red). (b) Relative likelihood of each model of climatic drivers in global total respiration, determined by the likelihood that each model minimizes the information loss measured by AIC.

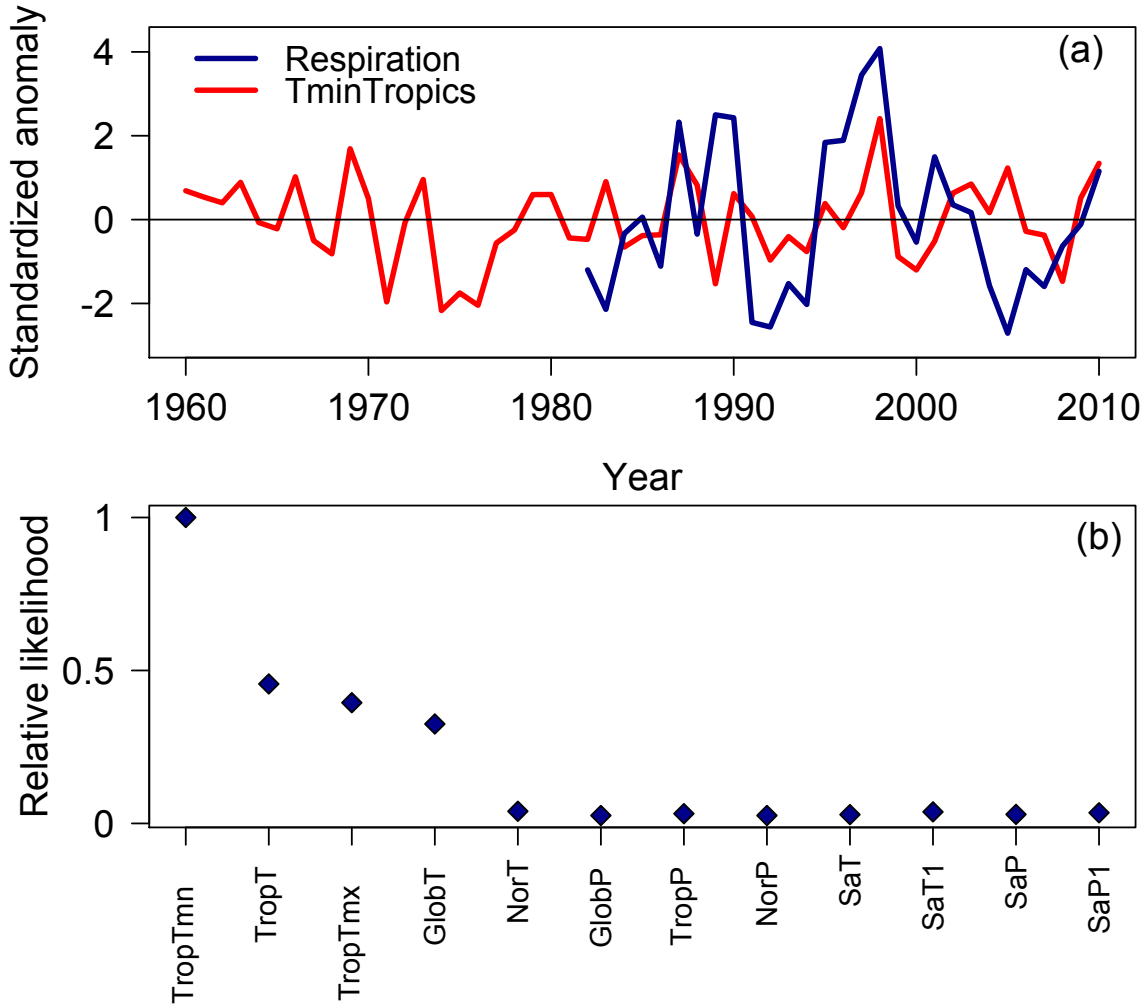

Figure S9: (a) Time-series of average minimum monthly temperature anomaly for the globe land surface (black) and tropical land surface (red). (b) Diurnal temperature range (DTR = Tmax – Tmin) for the globe land surface (black) and tropical land surface (red).

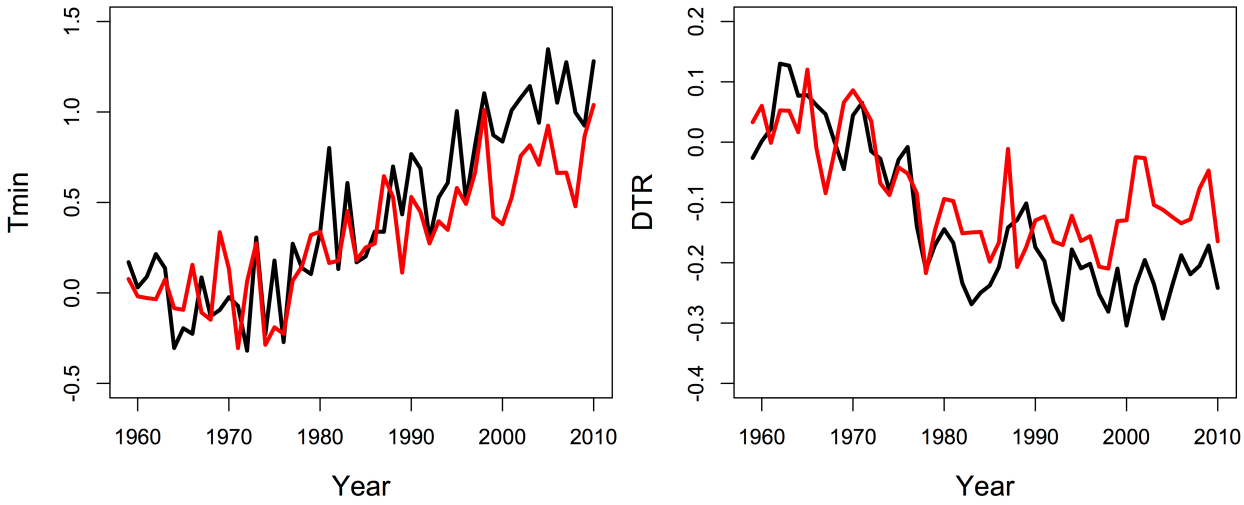

Figure S10: Emissions of C from CO_2 from 1959–2011, as estimated by several inventories, global models, and satellite-based products (see Methods). Each time-series is normalized to its mean.

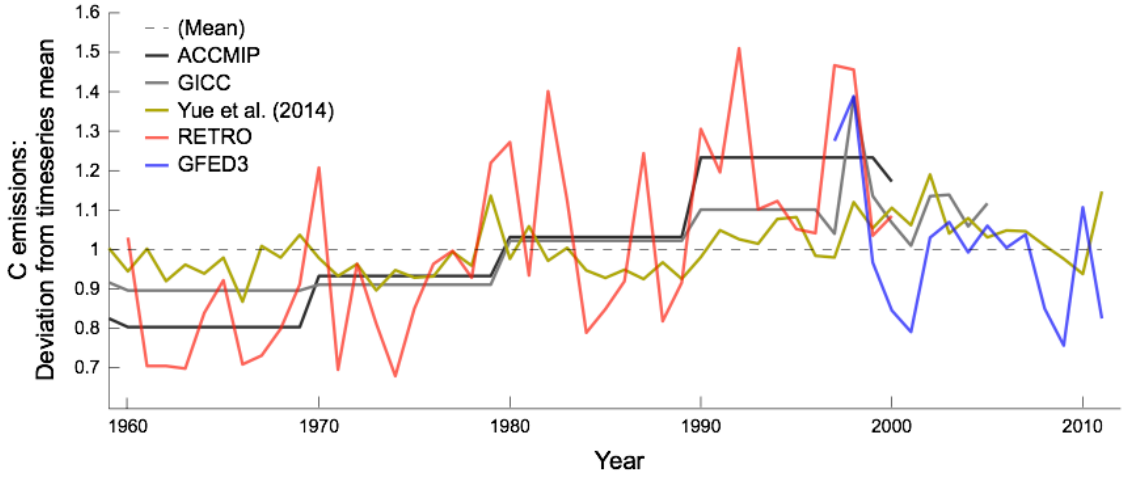

Figure S11: Emissions of C from fire from the (a) RETRO fire model from 1960–2000 and (b) the GFED3 database from 1998–2010 versus detrended terrestrial NEE anomalies.

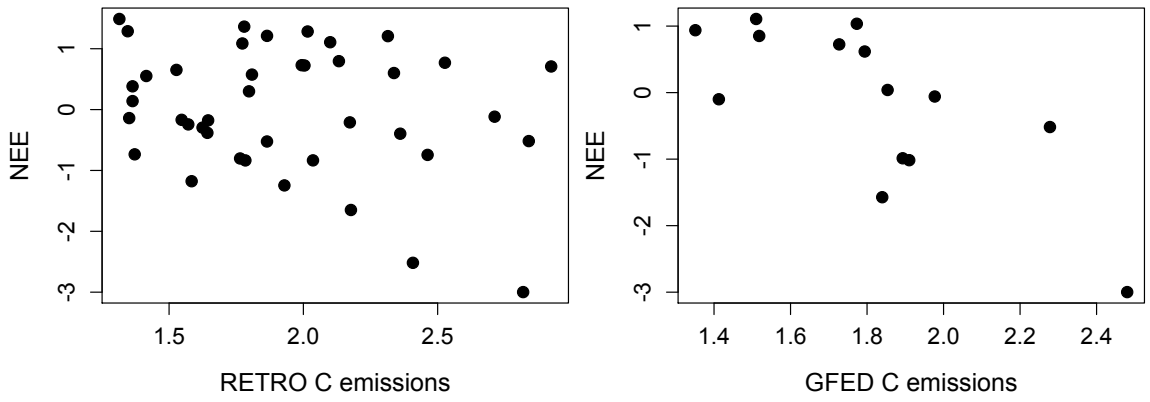

Figure S12: Comparison of Dec-Jan calculations (blue) of atmospheric growth rate (AGR) of carbon dioxide versus annual values (black) for the globe (left) and Mauna Loa (right).

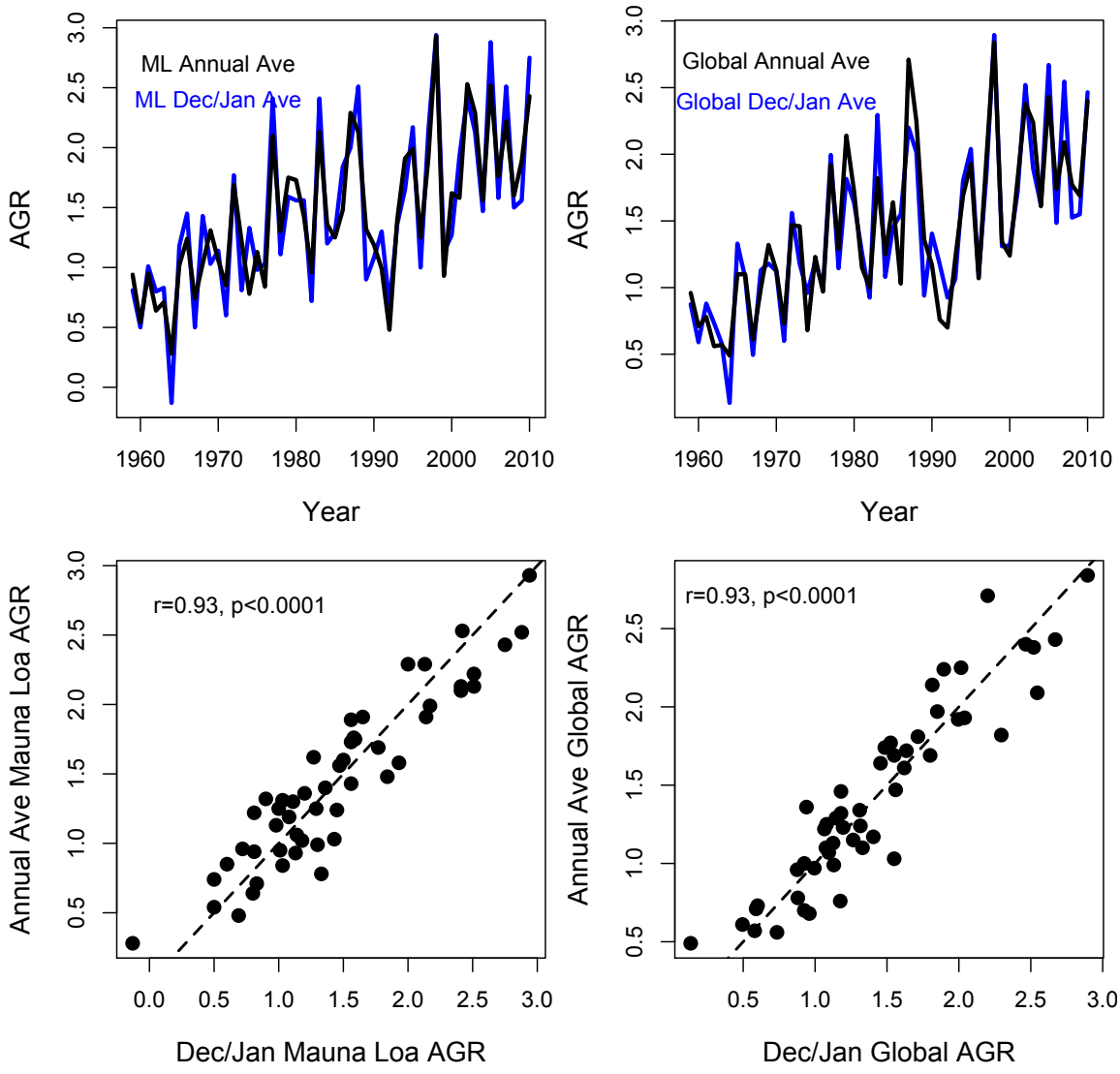

Figure S13: Land variance increases in both datasets of the land C sink (i.e., NEE), where ocean uptake is estimated either by the six AOGCMs from the Global Carbon Project (GCP; a-c) or by data assimilation (DA; d-f).